Available online at www.sciencedirect.com
SCIENCE DIRECT®
Microelectronic Engineering 75 (2004) 31–42
MICROELECTRONIC ENGINEERING
www.elsevier.com/locate/mee

Dielectrophoretic assembly and integration of nanowire devices with functional CMOS operating circuitry

S. Evoy [a,*], N. DiLello [a], V. Deshpande [a], A. Narayanan [b], H. Liu [c], M. Riegelman [c], B.R. Martin [d], B. Hailer [e], J.-C. Bradley [f], W. Weiss [d], T.S. Mayer [g], Y. Gogotsi [h], H.H. Bau [c], T.E. Mallouk [d], S. Raman [b]

[a] *Department of Electrical and Systems Engineering, The University of Pennsylvania, 200 S. 33rd St., Room 206, Philadelphia, PA 19104, USA*
[b] *Bradley Department of Electrical and Computer Engineering, Virginia Polytechnic Institute and State University, Blacksburg, VA 24061, USA*
[c] *Department of Mechanical Engineering and Applied Mechanics, The University of Pennsylvania, Philadelphia, PA 19104, USA*
[d] *Department of Chemistry, Pennsylvania State University, University Park, PA 16802, USA*
[e] *Department of Materials Science and Engineering, Virginia Polytechnic Institute and State University, Blacksburg, VA 24061, USA*
[f] *Department of Chemistry, Drexel University, Philadelphia, PA, 19104, USA*
[g] *Department of Electrical Engineering, Pennsylvania State University, University Park, PA 16802, USA*
[h] *Department of Materials Science & Engineering, Drexel University, Philadelphia, PA 19104, USA*

Received 31 July 2003; accepted 23 September 2003
Available online 26 February 2004

Abstract

We present a novel platform for the development and deployment of nanosensors in integrated systems. The nanosensor technology is based on "striped" high aspect ratio cylindrical structures grown using porous membranes as templates. These nanostructures are manipulated using dielectrophoretic forces, allowing their individual assembly and characterization. This assembly also enables the development of "mixed-mode" integrated circuits that include readout, signal processing, and communications circuitry, as well as the requisite layout for the post-IC assembly of the nanostructures. We report on preliminary designs of such mixed mode systems whose layouts integrate dielectrophoretic assembly sites with a rudimentary resistance read-out circuitry.
© 2004 Published by Elsevier B.V.

Keywords: Sensors; Nanometer structures; Integrated systems; Dielectrophoresis; Nano-assembly

1. Introduction

A microelectronics revolution is underway, defined by the integration of multifunctional materials into single-chip microsystems. These systems

* Corresponding author. Tel.: +1-215-898-7899; fax: +1-215-573-2068.
E-mail address: evoy@ee.upenn.edu (S. Evoy).

0167-9317/$ - see front matter © 2004 Published by Elsevier B.V.
doi:10.1016/j.mee.2003.09.010

will monolithically incorporate transistor-based electronics with micro- and nanomechanical actuators, micro-pumps and valves, physical, biological and chemical sensors. This integration offers tremendous advantages with respect to size, power consumption, and the batch processing necessary to support the low-cost deployment of "intelligent" microsystems. Specifically, the concept of cross-reactive sensor arrays represents a promising platform for the accurate analysis of analytes in complex mixtures by virtue of the varied response of different sensor elements within a large array [1]. Because of the analogy between the multiple sensor concept and biological olfaction, these arrays are popularly called electronic noses [2] (or tongues [3], etc.). In addition, there has been phenomenal growth in the availability of computational power and wireless communications capacity. These advanced information technologies are now poised to receive, process, store, and distribute large quantities of data about the physical world. For example, next-generation "smart" microsensors may be realized as multichip assemblies that include a sensor chip, control chips, and a micromachined corner-cube optical transmitter/detector for line-of-sight communications [4].

Many different sensing platforms have been developed for such concepts [5–24], including metal oxides [5] and other [6] chemoresistors, chemically sensitive field effect transistors (ChemFETs) [7–9], intrinsically conducting polymers [10], swelling polymers [11], mass-sensitive thickness shear resonators and surface acoustic wave devices [12–15], as well as capacitive [16], calorimetric [17–20], electrochemical [18,19], and fluorescent [20,21] microsensors. The bottom-up synthesis and integration of nanoscale structures open new opportunities for the development of such integrated sensor arrays with respect to reduced size and, more importantly, the power consumption of individual elements. For instance, different types of semiconductor nanowires have been synthesized by chemical or electrochemical growth [25,26] and are being considered as prototypes of electronic devices [27,28]. Alternatively, the intrinsic structure of carbon nanotubes offers a platform upon which functional nanoscale systems can be designed. Hybrid materials in which various molecules are encapsulated within single-wall carbon nanotubes (SWNTs) are now routinely being reported [29].

The ability to manipulate individual nanostructures is necessary for the characterization of their electrical and mechanical behavior, the analysis of their response to outside agents and stimuli, and, *more importantly*, for their eventual *integration* into multifunctional systems. Several techniques have been reported for the interfacing of nanostructures with circuitry. Earlier work involved random surface dispersion from solution, followed by the fabrication of electrodes at known nanotube locations [30–32]. In another technique, the tip of an AFM was used to manipulate and assemble nanotubes across contact pads [33,34]. These approaches enabled the demonstration of the first carbon nanotube devices. However, their very limited throughput precludes their viability as a manufacturing technology.

Following the pioneering work of Pohl [35], we and others have used non-uniform electric fields to manipulate rod-shaped particles that are suspended in liquid media [36–38]. For instance, Smith et al. [38] reported the placement of gold nanowires using dielectrophoretic forces generated by buried electrodes, and Evoy et al. [39] used this technique to integrate mechanically resonant suspended Rh nanorods onto Si circuits. More recently, the dielectrophoretic assembly of SWNTs has been reported [40], demonstrating its viability for the integration of functionalized nanotubes.

While dielectrophoretic trapping therefore represents a potent tool for the characterization of individual nanostructures, it also offers the important advantage of being compatible with established integrated circuit (IC) fabrication processes. Indeed, the metal layers available in modern silicon foundry processes can be leveraged to define the electrodes necessary for the *post-IC* assembly of nanosensors (Fig. 1). We therefore envision "mixed-mode" circuits that will include readout, signal processing, and communications circuitry, as well as the requisite circuitry necessary to perform the post-IC assembly of the nanostructures.

This report describes the platform used for the synthesis of nanosctructures, then moves on to a

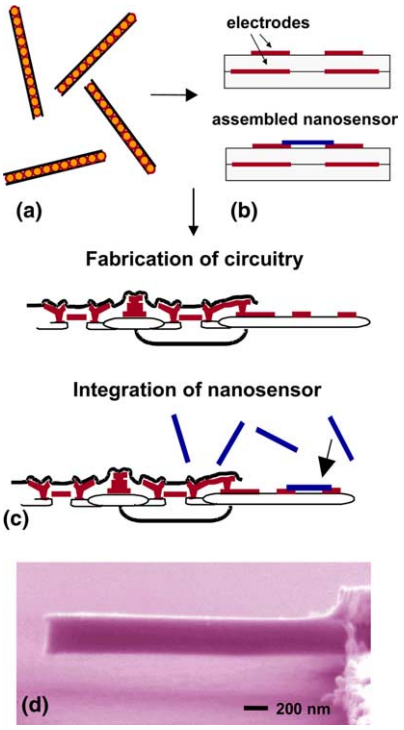

Fig. 1. Bottom-up synthesis and integration of functional nanostructures. (a) Structures are produced from the bottom-up using templated growth technologies. (b) Dielectrophoretic forces are used to assemble the nanostructure on prefabricated circuit. (c) Compatible with standard IC manufacturing technologies, this approach enables the design of microchips containing operating circuitry as well as the necessary layout for the post-IC assembly on the nanosensor onto predefined sites. (d) Assembled of Rh nanomechanical cantilever on a Si circuit.

theoretical description of dielectrophoretic assembly. The trapping and characterization of metallic rods and carbon tubes is then described. We then conclude by presenting preliminary designs of mixed mode systems whose layouts integrate dielectrophoretic assembly sites with a rudimentary resistance read-out circuitry.

2. Development of functional nanostructures through templated growth techniques

The nanosensor technology employed here is based on ''striped'' high aspect ratio cylindrical structures grown using porous membranes (alumina or polycarbonate) as templates. These kinds of structures follow from the extensive studies of Moskovits and co-workers [41], Martin [42], and others over the last two decades. Commercially available (or easily synthesized) membranes containing 10^8–10^{10} pores/cm^2 are replicated electrochemically, and the membranes are then dissolved to give suspensions of freestanding nanowires. Monodisperse collections of wires with diameters in the range of 30–300 nm and lengths of several microns are routinely attained. By interrupting the plating process, changing the plating solution, and/or introducing self-assembly reactions between plating steps, it is possible to make many different kinds of structures in which composition is controlled along the length or around the circumference of the nanowire.

Here, commercial anodized alumina membranes (Whatman Anodisc) with internal pore diameters ranging between 250 and 450 nm were prepared for electrodeposition by first thermally evaporating ~150 nm of Ag onto one of their sides. An additional 5 μm of Ag (Technic 1025 plating solution) was then galvanostatically deposited in order to fill pinhole defects. The pores of the membrane were then filled with approximately 10 μm of Ag by flowing 5 C at 2 mA/cm^2 with respect to the membrane area. This layer prevented electrodeposition of the metal in the defective outer layers of the membrane. The membrane was then transferred to an ice-cooled ultrasonic bath. This bath served to increase the diffusion rate of plating solution, and to minimize surface adsorbants. Rhodium was electroplated from an acidic solution at a current density of 1.2 mA/cm^2 for 90 min. The membrane is then thoroughly rinsed with water, the silver dissolved in 5 M nitric acid, and the rods released by dissolving the alumina in 5 M NaOH. The process results in Rh rods with average length of 3–6 μm. The rods are then rinsed by centrifugation, and removing the supernatant through pipetting. The rods are then resuspended in isopropanol in preparation for assembly.

This templated growth technology was employed for the design and development of functional nanostructures. For instance, nanomechanical magnetic sensors were produced by

capping the Rh rod with an additional 25 nm of electroplated Ni, followed by an additional 100 nm of protective Au (Fig. 2(b)). Magnetic force microscopy confirms the presence of a magnetically active nanostructure at the extremity of the non-magnetic support rod. In addition, the technology is also being employed for the synthesis of functional Au/SnO_2/Au chemresistive nanostructures, designed for the development of a nanostructure array-based volatile organic compound sensing microsystem. In this case, a sequence of Au, Sn, and Au electroplating has been employed prior to dissolution of the membrane (Fig. 2(c)). Conversion of the Sn segment into SnO_2 is to be achieved through oxidation, either prior or after release from membrane.

Finally, a similar approach has been used for the production of carbon tubes (Fig. 2(d)) [43]. In this case, a similar membrane (Whatman Anodisc, 13 mm diameter) was placed in a quartz reaction vessel. The reaction vessel was placed in a tube furnace, and Ar gas was flowed at a rate of 20 sccm. The temperature was then ramped to 670 °C. Once the temperature stabilized at 670 °C the gas flow was switched to a premixed mixture of 30% ethylene and 70% helium at a flow rate of 20 sccm. The reaction was left for ~6 h, after which the flow was switched back to Ar at a rate of 20 sccm. A piece was placed in a glass test tube (18 mm wide and 150 mm long), and the membrane dissolved through sonication in a 1 M NaOH solution. The resulting suspension of carbon tubes was filtered through a polyester nuclear track etched membrane with 100 nm pores. The carbon tubes were washed by pouring through 15 ml of hot water (75 °C measured using IR thermometer), and then 15 ml of acetone over the nanotubes. Once dry the membrane with the nanotubes was placed in a glass vial, and 3 ml of acetone was added. The vial was held in a bath sonicator for ~20 s to disperse the tubes. The resulting tube diameters range from 250 to 600 nm, and their wall thickness is approximately 15 nm, as measured through transmission electron microscopy.

3. Dielectrophoretic assembly: Theoretical background

Dielectrophoresis (DEP) is defined as the motion of uncharged, polarizable particles in a non-uniform electric field [44]. The dielectrophoretic

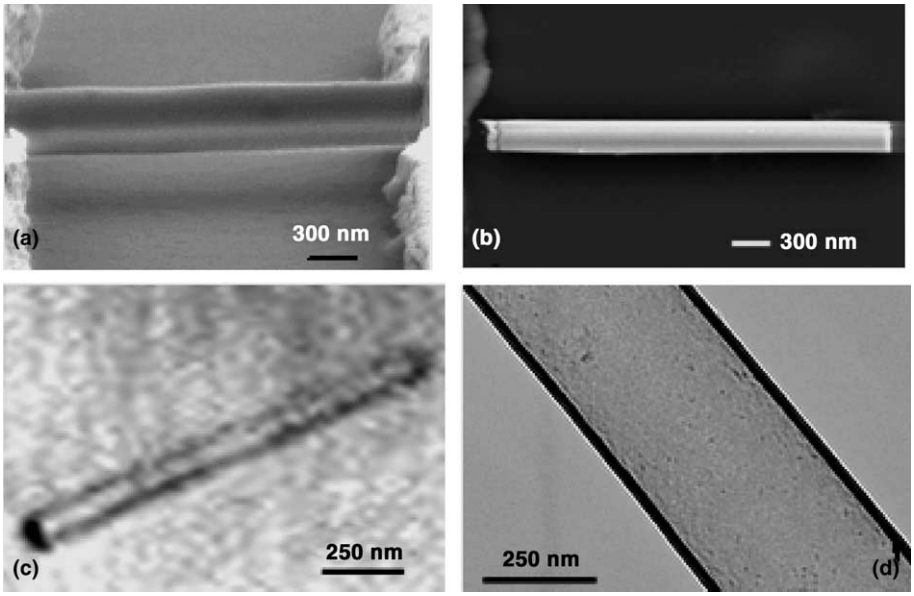

Fig. 2. Nanostructures produced through templated growth technology. (a) SEM image of an assembled rhodium rod. (b) SEM image of a Rh/Ni/Au nanomechanical magnetic sensor. (c) SEM image of a segmented Au/Sn/Au structure. (d) TEM image of a carbon tube.

forces result from the interaction of the electric field with a dipole induced in the particles. Depending on the particles' and the medium's dielectric properties, the motion is directed either toward (positive DEP) or away from (negative DEP) regions of high electric field intensity. While DEP occurs under both DC and AC electric fields, AC fields are often preferred in order to suppress undesired electrochemical interactions at the electrodes' surfaces, to suppress electrophoresis, and to eliminate motion due to the particles' electric charge. In addition, the use of AC potential allows for a two-layer capacitive actuation of the electrodes, which prevents the electrodes and particles from burning out when the gap between two electrodes is bridged [38]. One can readily control the direction of the electric field by judicious patterning of the electrodes on the substrate. High-intensity electric fields are readily obtained with relatively low potential differences given the small electrode gaps involved.

The dielectrophoretic force is usually approximated through its first dipole moment contribution [45]

$$\mathbf{F} \sim c\varepsilon_0\varepsilon_m V_p \mathrm{Re}(f_{CM})\nabla|\mathbf{E}_{rms}^2|, \tag{1}$$

where $\mathbf{E}$ is the electric field; ε_0 and ε_m are, respectively, the dielectric constant of free space and the relative dielectric constant of the suspending liquid, V_p is the particle's volume, c is a numerical coefficient on the order of unity, and $\mathrm{Re}(f_{CM})$ is the real part of the relative particle polarization (i.e. the Clausius-Mossotti factor). Both c and f_{CM} depend on the particle's geometry. For example, in the case of a spherical particle, $f_{CM} = (\varepsilon_p^* - \varepsilon_m^*)/(\varepsilon_p^* + 2\varepsilon_m^*)$ and $c = 3/2$, where ε_m^* and ε_p^* are the complex permittivities of the particle and of the medium, respectively; $\varepsilon^* = \varepsilon - j(\sigma/\omega)$; and σ is the electric conductivity.

The dipole moment approximation is valid only when the dimensions of the particle are much smaller than the characteristic length scale of the electric field. Since this is often not the case in micron scale devices, a Maxwell stress tensor must be used to calculate the forces [46].

The surface force density $\mathbf{f}$ is given by the following equation:

$$\mathbf{f} = \varepsilon_0\varepsilon_m\left(\mathbf{E}(\mathbf{E}\cdot\hat{n}) - \frac{1}{2}(\mathbf{E}\cdot\mathbf{E})\hat{n}\right), \tag{2}$$

where $\hat{n}$ is the outer unit vector normal to the particle's surface. When the particle is conductive, Eq. (2) simplifies to

$$\mathbf{f} = \frac{1}{2}\varepsilon_0\varepsilon_m(\mathbf{E}\cdot\mathbf{E})\hat{n} = \frac{1}{2}\varpi\mathbf{E}, \tag{3}$$

where ϖ is the electric charge's density on the conductor's surface. Forces and torques are, respectively, obtained from the integration of the force density and the cross-product of the force density directed from the particle's center of mass to a point on the particle's surface. The integration is performed over the surface of the entire particle. For example, the total force acting on the particle is expressed as

$$\mathbf{F} = \int_S \mathbf{f}\,\mathrm{d}S. \tag{4}$$

Wang et al. [47] have shown that Eq. (1) is the leading term in a Taylor series expansion of the electric field with respect to the distance from the particle's center of mass.

In absence of dissipative processes, the forces and torques can also be calculated from the virtual work principle. In this approach, the total electric energy stored in the system is written as

$$U = \frac{1}{2}\int_{\mathrm{system}} \mathbf{D}\cdot\mathbf{E}\,\mathrm{dV}, \tag{5}$$

where $\mathbf{D}$ is the displacement vector. The integration is carried out over the volume of the entire system. The force is then given by

$$\mathbf{F} = -\nabla U. \tag{6}$$

Here, we are interested in trapping nanorods, nanotubes, and nanofibers in a gap between two electrodes (Fig. 3). Since the size of the object is comparable to the length scale of the electric field (about the gap size between the electrodes), the dipole moment approximation is not likely to provide accurate results. The Maxwell tensor and virtual work approaches are instead being used. The potential field is first calculated using the FEMLAB electromagnetic package [48]. Fig. 3 depicts the layout of the simulation. A two-dimensional cylindrical particle of length L, width

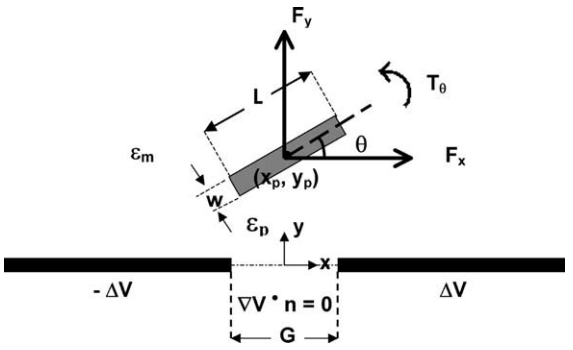

Fig. 3. Schematic description of the model used to calculate the dielectrophoretic and viscous forces acting on the cylinder and the motion of the cylinder.

W, and relative dielectric constant ε_p is submerged in a liquid drop of dielectric permittivity ε_m. The liquid is assumed to be a perfect dielectric. The center of mass of the particle is located at $\{x_p, y_p\}$, and the particle is inclined at angle θ with respect to the horizontal (x) axis. Two electrodes (heavy solid lines in Fig. 3), separated by a gap G, are patterned on the surface. The left and right electrodes are equipotential surfaces at potentials ΔV and $-\Delta V$, respectively. The gap between the electrodes is a perfect dielectric. The liquid drop is large compared to the particle's size, and its outer boundaries are electrically insulated. Fig. 4 depicts the results of the calculations when the particle is located at $\{x_p, y_p, \theta_p\} = \{0, 10\ \mu m, 30°\}$. $L = 10\ \mu m$, $W = 1\ \mu m$, $G = 5\ \mu m$, $\varepsilon_p = 100$, $\varepsilon_m = 10$, and $\Delta V = 1$ V. The contour lines correspond to constant potential lines and the colors correspond to various potential values.

The DEP force field is then evaluated from Eq. (6). The x- and y-direction DEP forces are -3.4×10^{-7} and -1.7×10^{-6} N, respectively. The torque is -5.9×10^{-13} N m. The torque is defined as positive in the counterclockwise direction. We verified that the force calculations based on the virtual work are, indeed, consistent with results obtained by integrating the Maxwell stress tensor on a closed surface around the particle. We also constructed a few test cases that we were able to solve analytically and verified the numerical results by comparison with analytical solutions [49].

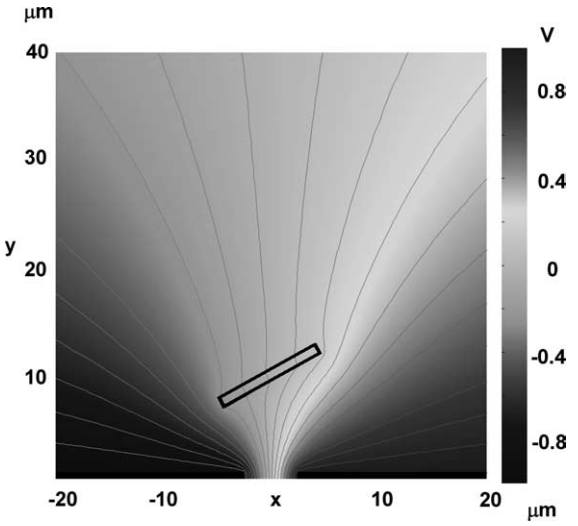

Fig. 4. Finite element calculations of the potential field and the dielectrophoretic forces acting on a particle submerged in a drop of perfectly dielectric liquid.

In order to predict the particle's trajectory, we calculated the drag force. Since the Reynolds number associated with the DEP motion is typically small, we neglected inertial effects and modeled the motion as Stokes flow. In such an approximation, one can compute the drag tensor $\mathbf{T_D}$ such that the drag is given by

$$\mathbf{D} = \mathbf{T_D}\frac{d\mathbf{x}}{dt}, \tag{7}$$

where $\mathbf{D}^T = \{D_x, D_y, D_\theta\}$ and the superscript T denotes transpose. These calculations were carried out with the chemical engineering package in Femlab. The particle's equations of motion are calculated by equating the viscous forces with the DEP forces. The particle's trajectory is then obtained by solving the ordinary differential equations

$$\mathbf{T_D}\frac{d\mathbf{x}}{dt} = \mathbf{F}_{DEP}. \tag{8}$$

4. Assembly and characterization of nanostructures

4.1. Experimental techniques

Individual nanostructures were positioned onto lithographically defined electrodes fabricated on a

silicon wafer (Fig. 5). First, a 500 nm electrically insulating SiO_2 layer was grown using thermal oxidation at 950 °C. The first set of electrodes was patterned out of a 190 nm layer of Au, with an underlying 10 nm layer of Cr, using photolithography and lift-off. The electrodes were then buried under 150 nm of sputter-deposited SiO_2. The top capacitive electrodes were fabricated in a 100-nm thick metal layer. While a first generation employed Au [39], we have here opted for a stiffer Ni/Cr alloy to provide better a mechanical support. A total of 100 assembly sites exist per chip, with gap spacings varying from 5 to 30 μm.

Using an approach developed by Smith et al. [38], the assembly electrodes are capacitively driven by feeding an assembly signal between the sets of buried electrodes for 5 min. This assembly signal is provided by a Topward 8110 function generator, and amplified by a Bogen GA-6A amplifier. The optimal AC amplitudes for assembly were 10 and 45 V_{pp} for the Rh nanorods, and carbon tubes, respectively. Following assembly, a final lithography step is performed to deposit 100-nm thick "clamping" electrodes that will hold the structure in place, and provide electrical contacts through contact pads. The structures are then released in a buffered 6:1 HF solution for 2 min. The pictures of an assembled Rh nanorod and a carbon tube are shown in Fig. 6.

The *I–V* responses of the devices were probed in ambient in a two-terminal configuration using a Hewlett–Packard 4145B Semiconductor Parameter Probe Station. The temperature of the device was raised using a Powerstat Variable Autotransformer (type 3PN116B), which heated up the metal platform that the wafer rests.

4.2. Assembly and characterization of Rh nanorods and carbon tubes

Fig. 7 depicts a typical *I–V* response of a Rh rod assembled across a $L = 5$ μm gap at room temperature. The slope of this line yields an apparent conductance of $S = 3.6$ mS ($R = 277$ Ω).

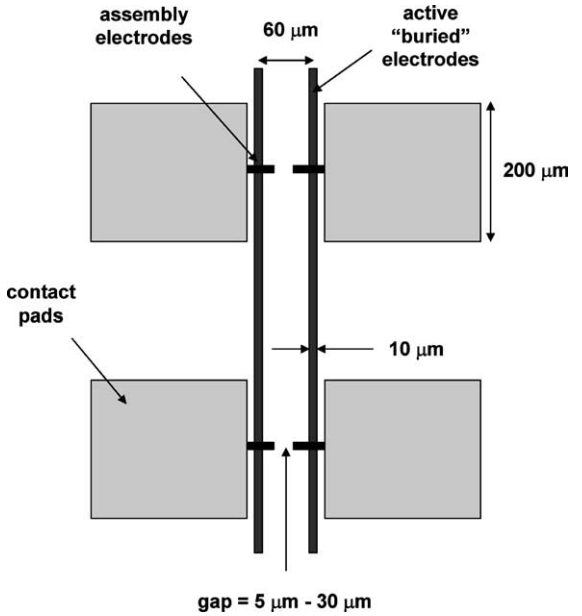

Fig. 5. Layout of assembly electrodes employed for the dielectrophoretic trapping and characterization of nanostructures. The assembly signal is fed to a pair of active electrodes buried under 150 nm of SiO_2. The signal is capacitively coupled to a pair of top assembly electrodes. Following assembly, a pair of contact pads is fabricated for electrical testing purposes.

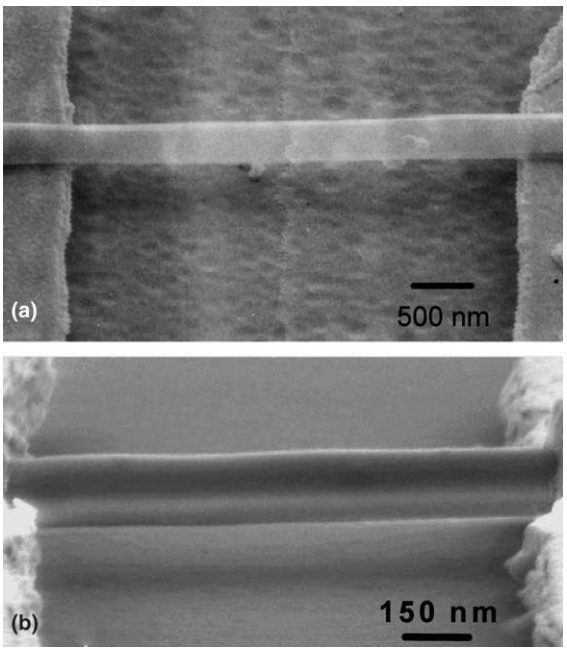

Fig. 6. Scanning electron micrographs of assembled and released structures: (a) Carbon tube. (b) Rhodium rod.

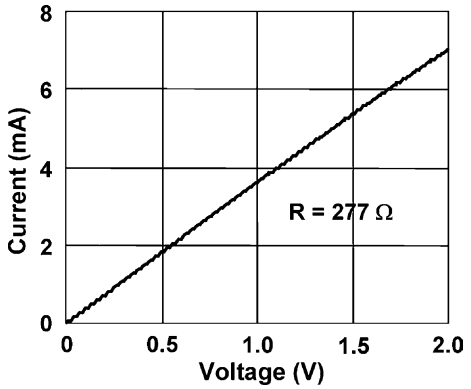

Fig. 7. Current/voltage characteristic of assembled Rh rod. The diameter and length of the structure was $D = 300$ nm and $L = 5$ μm, respectively.

Given the reported resistivity of Rh ($\rho = 4.3$ μΩ cm), [50] a gap length of 5 μm, and an approximate diameter of $D = 300$ nm, one would rather have expected a resistance in the $R = 10$ Ω range. This discrepancy could indicate dominance of contact resistance in the I–V measurements at these ranges. The typical temperature-dependant I–V behavior of a carbon nanopipe is then reported in Fig. 8. Typical conductances show a steady increase as the temperature increases, from $G = 5$ μS ($R = 200$ kΩ) at room temperature, to $G = 10$ μS ($R = 100$ kΩ) at 125 °C. The bulk resistivity of CVD graphite is reported to be in the 500 μΩ cm in the ab plane, but can be as high 3×0^5 μΩ cm in the c-direction [51]. A 15 μm long tube with outer diameter of 300 nm and wall thickness of 15 nm (as measured through TEM), whose axis would coincide with a dominant c-axis crystalline orientation, could therefore theoretically have a resistance as high as $R = 600$ kΩ, within the range of our experimental data. However, the high resistivity observed could rather be explained by the disordered wall structure of the pipes produced by CVD at moderate temperatures. Graphene sheets in the thin tube walls are not expected to be continuous, thus potentially causing the high resistance. Finally, the contribution of contact point resistance in such two-probe configuration should also be considered.

Our data also shows a substantial decrease of resistance as temperature is ramped from room

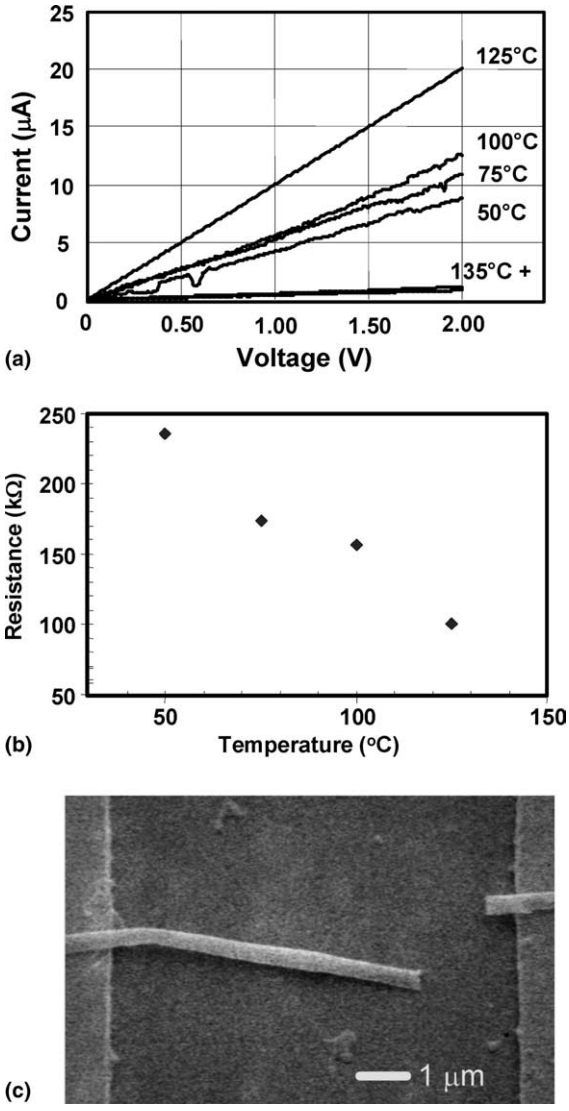

Fig. 8. (a) Current/voltage characteristic of assembled carbon tube at various temperature. An irreversible increase of conductance is seen with moderate temperature increases to $T = 125$ °C. (b) Corresponding resistance values extracted from linear fit of data. (c) Heating above $T = 135$ °C invariably results in the mechanical failure of the pipes.

temperature to $T = 125$ °C (Fig. 8(b)). However, this increase of conductance is not reversible as temperature is ramped back down. Such phenomenon could be the result of some annealing of the anchor points, or of the pipes themselves. Finally, further increase to a temperature above

135 °C results in a mechanical failure of the tube and a permanent disruption of the conductivity (Fig. 8(c)). Although thermomechanical mismatch could be at play, the similar thermal expansion coefficients of the pipes and substrate ($\alpha = 2.55 \times 10^{-6}$ K^{-1} for Si [52] vs. $\alpha = 2.3 \times 10^{-6}$ K^{-1} for graphite [51]) suggest that other thermally activated degradation processes should also be considered. To that end, we are planning to repeat these experiments under controlled atmosphere to identify and isolate any possible interaction with atmospheric gases as possible cause of these observations.

4.3. Discussion

Dielectrophoretic assembly has enabled the electromechanical characterization of individual elements developed. Contact resistance is suspected to have dominated the measured two-terminal electrical responses of Rh structures. Further work in under way to improve contact resistance through development of a post-assembly anneal. In addition, the segmented growth technology employed here has already allowed the development of striped nanowires consisting of a central segment terminated by two metallic extremities (Fig. 2(c)). Further development of such gold-terminated structures would allow the assembly of functional devices in which the metal/metal contact point would represent a negligible contribution compared to the eventual chemresistive functional response of the centrally suspended non-metallic segment.

5. Integration with CMOS operating circuitry

Dielectrophoretic trapping offers the important advantage of potentially being compatible with established IC fabrication processes. Indeed, the metal layers available in modern silicon foundry processes can be leveraged to define the electrodes necessary for the *post-IC* assembly of nanosensors. We therefore envision "mixed-mode" integrated circuits that will include readout, signal processing, and communications circuitry, as well as the layout necessary to perform the *post-IC* assembly of the nanostructures. We present here the preliminary design of such a hybrid circuit.

The layout of the assembly sites and the integrated readout circuit was implemented using the Motorola HiP6WRF low-voltage 0.18 μm Si/SiGe BiCMOS process [53]. Only the CMOS platform technology is being utilized in this work. Here, the metal layers M4 and M5, and the dielectric that separates them form the necessary AC coupling capacitors (Fig. 9). The chip design also calls for the opening of the top passivation layer to expose the top metal layer in the assembly area to allow assembly of the nanowires. Two types of designs were implemented. In the first, output lines are directly connected to the bonding pads to demonstrate the assembly of nanowires on an IC, while the other has output lines connected to a CMOS readout circuit to demonstrate integration of nanoscale metal wires with the VLSI circuit. Each family has sixteen assembly sites providing different spacing widths between the upper electrodes. The gap between the assembly electrodes varies from 3.0 to 6.2 μm. The structures, once assembled, are connected to the bond pads or readout

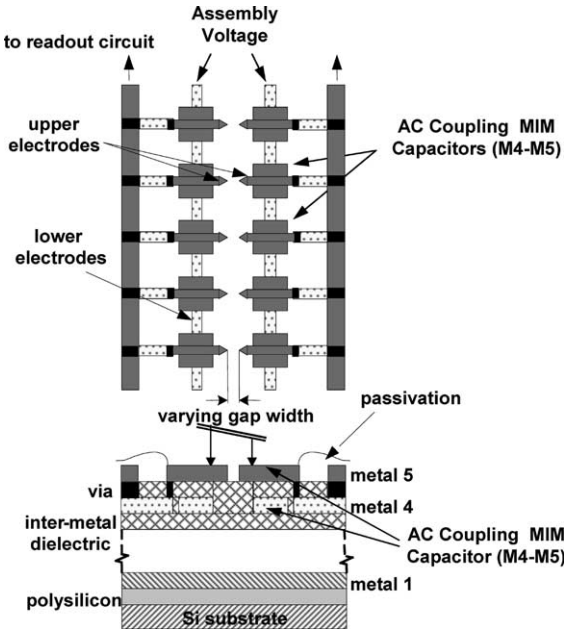

Fig. 9. Layout of assembly electrodes in Motorola HiP6WRF low-voltage 0.18 μm Si/SiGe BiCMOS process.

circuit through vias and M4 interconnects (Fig. 9). After assembly, the nanowires will bridge the gap between the top electrodes and will act as one arm of a Wheatstone bridge within a readout circuit discussed below.

For proof-of-concept purposes, a simple circuit was designed in CMOS technology to read out the resistance of the assembled devices. The circuit consists of a basic Wheatstone bridge network with three known resistance values and a CMOS two-stage differential amplifier to amplify the output of the resistance bridge to a measurable voltage. A schematic representation of the readout circuit is given in Fig. 10. The unknown resistance (R_X) in this case is the assembled nanowires. The resistance of the nanowires is the output parameter, which is measured in the form of voltage, V_{OUT}. The relation between the output voltage, V_{OUT} and the unknown resistance, R_X can be deduced from the following equation:

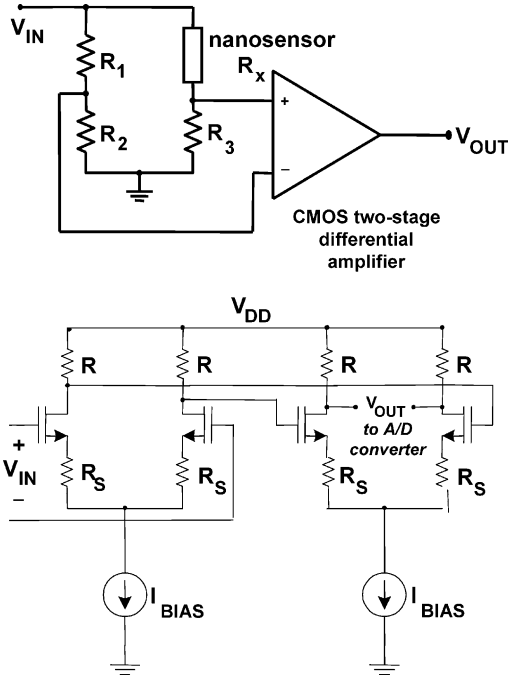

Fig. 10. Schematic representation of Wheatstone bridge circuitry employed for resistance readout of assembled nanostructures.

$$(V_{OUT}/V_{IN}) = \alpha[(R_1/(R_1+R_2)) - (R_X/(R_3+R_X))], \quad (9)$$

where α is the gain of the differential amplifier.

The supply voltage for the readout circuit is 1.8 V. The MOS transistors used in the differential stages are multifingered devices with a gate width of 100 m. A bias current $I_{BIAS} = 270$ μA is provided to the differential stages by a CMOS current source. The output voltage could then eventually be digitized using a low-power A/D converter before data transmission.

6. Summary

We have presented an integrated platform for the development, assembly and integration of functional nanostructures with standard CMOS operating circuitry. This platform is based on the bottom-up synthesis of functional nanostructures produced through a templated growth method, and their assembly onto prefabricated circuits using dielectrophoretic forces.

Dielectrophoretic assembly enables the electromechanical characterization of individual elements. Contact resistances are expected to have dominated the measured two-terminal electrical responses of Rh structures. Further work in under way to improve contact resistance through development of a post-assembly anneal. Our segmented growth technology has already allowed the development of striped nanowires consisting of a central functional segment terminated by two metallic extremities. Further development of such gold-terminated structures would allow assembly of devices in which the metal/metal contact point would represent a negligible contribution compared to the chemresistive response of the central segment.

Preliminary designs of mixed-mode systems that integrates dielelectrophoretic assembly sites with operating circuitry were presented. A simple circuit was designed in CMOS technology to perform the readout of the resistance of assembled nanowires. These initial designs represent the first step towards the development of a vertically

integrated platform for the deployment of functional nanostructures in integrative systems.

Acknowledgements

A. Narayanan, S. Evoy, and S. Raman acknowledge funding from NSF collaborative research awards #ECS-0225439 and #ECS-0225496. They also thank Motorola Semiconductor Products Sector, Austin, TX, in particular Chris Magnella and Michael Clifford, for providing access to their HIP6W 0.18 μm BiCMOS technology for this project. N. DiLello and V. Deshpande have received summer salary support from NSF REU program #EEC-0244055.M. Riegelman, J.C. Bradley, Y. Gogotsi, and H.H. Bau are supported by NSF NIRT program #CTS-0210579. H. Liu and H.H. Bau are supported by DARPA SIMBIOS program N66001-01-C-8056. M. Riegelman also acknowledges further support from a GAANN fellowship. Transmission electron microscopy of carbon tubes was performed by Dr. H.Ye.B.R. Martin, W. Weiss, T.E. Mallouk, and T.S. Mayer were supported by DARPA and ONR under contract N00014-01-10659.

References

[1] K.J. Albert, N.S. Lewis, C.L. Schauer, G.A. Sotzing, S.E. Stitzel, T.P. Vaid, D.R. Walt, Chem. Rev. 100 (2000) 2595–2626.
[2] A.J. Matzger, C.E. Lawrence, R.H. Grubbs, N.S. Lewis, J. Comb. Chem. 2 (2000) 301–304.
[3] J.J. Lavigne, S. Savoy, M.B. Clevenger, J.E. Ritchie, B. McDoniel, S.-J. Yoo, E.V. Anslyn, J.T. McDevitt, J.B. Shear, D. Neikirk, J. Am. Chem. Soc. 120 (1998) 6429–6430.
[4] K. Bult, A. Burstein, D. Chang, M. Dong, M. Fielding, E. Kruglick, J. Ho, F. Lin, T.-H. Lin, W.J. Kaiser, H. Marcy, R. Mukai, P. Nelson, F.L. Newberg, K.S.J. Pister, G. Pottie, H. Sanchez, O.M. Stafsudd, K.B. Tan, C.M. Ward, S. Xue, J. Yao, in: Proceedings International Symposium on Low Power Electronics and Design, Monterey, CA, August 1996, pp. 17–21.
[5] K.C. Persaud, G. Dodd, Nature 299 (1982) 352.
[6] Q.Y. Cai, E.T. Zellers, Anal. Chem. 74 (2002) 3533–3539.
[7] J. Janata, in: J. Janata, R.J. Huber (Eds.), Solid State Chemical Sensors, Academic Press, New York, 1985, pp. 65–118.
[8] T. Eklov, I. Lundstrom, Anal. Chem. 71 (1999) 3544–3550.
[9] L.-G. Ekedahl, M. Eriksson, I. Lundstrom, Acc. Chem. Res. 31 (1998) 249–256.
[10] P.N. Bartlett, J.W. Gardner, R.G. Whitaker, Sensors Actuators A 23 (1990) 911–914.
[11] M.E. Koscho, R.H. Grubbs, N.S. Lewis, Anal. Chem. 74 (2002) 1307–1315.
[12] J.W. Grate, Chem. Rev. 100 (2000) 2627–2648.
[13] E.T. Zellers, J. Park, T. Hsu, W.A. Groves, Anal. Chem. 70 (1998) 4191–4201.
[14] A. Hierlemann, E.T. Zellers, A.J. Ricco, Anal. Chem. 73 (2001) 3458–3466.
[15] J. Park, W.A. Groves, E.T. Zellers, Anal. Chem. 71 (1999) 3877–3886.
[16] G. Niebling, A. Schlachter, Sensors Actuators B 27 (1995) 289–292.
[17] N. Abedinov, P. Grabiec, T. Gotszalk, Tz. Ivanov, J. Voigt, I.W. Rangelow, J. Vac. Sci. Tech. A 19 (2001) 2884–2888.
[18] S.R. Johnson, J.M. Sutter, H.L. Engelhardt, P.C. Jurs, J. White, J.S. Kauer, T.A. Dickinson, D.R. Walt, Anal. Chem. 69 (1997) 4641–4648.
[19] T.A. Dickinson, K.L. Michael, J.S. Kauer, D.R. Walt, Anal. Chem. 71 (1999) 2192–2198.
[20] N.A. Rakow, K.S. Suslick, Nature 406 (2000) 710–713.
[21] M. Otto, J.D.R. Thomas, Anal. Chem. 57 (1985) 2647–2651.
[22] K.R. Beebe, D. Uerz, J. Sandifer, B.R. Kowalski, Anal. Chem. 60 (1998) 66–71.
[23] S.M. Drew, D.E. Janzen, C.E. Buss, D.I. MacEwan, K.M. Dublin, K.R. Mann, J. Am. Chem. Soc. 123 (2001) 8414–8415.
[24] X. Song, J. Nolan, B.I. Swanson, J. Am. Chem. Soc. 120 (1998) 11514–11515.
[25] J.D. Holmes, K.P. Johnston, R.C. Doty, B.A. Korgel, Science 287 (2000) 1471.
[26] T. Thurn-Albrecht et al., Science 290 (2000) 2126.
[27] Y. Huang, X.F. Duan, Q.Q. Wei, C.M. Lieber, Science 291 (2001) 630.
[28] Y. Cui, Q.Q. Wei, H.K. Park, C.M. Lieber, Science 293 (2001) 1289.
[29] D.E. Luzzi, B.W. Smith, in: D. Tomanek, R.J. Enbody (Eds.), Science and Application of Nanotubes, Kluwer Academic/Plenum, New York, 2000, pp. 67–76.
[30] S.J. Tans, M.H. Devoret, H. Dai, A. Thess, R.E. Smalley, L.J. Geerligs, C. Dekker, Nature 386 (1997) 474.
[31] R. Martel, T. Schmidt, H.R. Shea, T. Hertel, Ph. Avouris, Appl. Phys. Lett. 73 (1998) 2447.
[32] K. Ishibashi, M. Suzuki, T. Ida, Y. Aoyagi, Appl. Phys. Lett. 79 (2001) 1864.
[33] L. Roschier, J. Penttila, M. Martin, P. Hakonen, M. Paalanen, U. Tapper, E.I. Kauppinen, C. Journet, P. Bernier, Appl. Phys. Lett. 75 (1999) 728.
[34] J. Lefebrvre, J.F. Lynch, M. Llaguno, M. Radosavljevic, A.T. Johnson, Appl. Phys. Lett. 75 (1999) 3014.
[35] H.A. Pohl, J. Appl. Phys. 22 (1951) 869–871.
[36] B.M.I. van der Zande, G.J.M. Koper, H.N.W. Lekkerkerker, J. Phys. Chem. B 103 (1999) 5754.

[37] B.R. Martin, D.J. Dermody, B.D. Reiss, M. Fang, L.A. Lyon, M.J. Natan, T.E. Mallouk, Adv. Mater. 12 (1999) 1021.
[38] P.A. Smith, C.D. Nordquist, T.N. Jackson, T.S. Mayer, B.R. Martin, J. Mbindyo, T.E. Mallouk, Appl. Phys. Lett. 77 (2000) 1399.
[39] S. Evoy, B. Hailer, M. Duemling, B.R. Martin, T E. Mallouk, I. Kratochvilova, T.S. Mayer, MRS Symp. Proc., 687 (Materials Science of Microelectromechanical Systems (MEMS) Devices IV), 2002, pp. 63–68.
[40] L.A. Nagahara, I. Amlani, J. Lewenstein, R.K. Tsui, Appl. Phys. Lett. 80 (2002) 3826.
[41] D. Al-Mawlawi, C.Z. Liu, M. Moskovits, J. Mater. Res. 9 (1994) 1014–1018;
D. Routkevitch, T. Bigioni, M. Moskovits, J.M. Xu, J. Phys. Chem. 100 (1996) 14037–14047.
[42] C.R. Martin, Science 266 (1994) 1961–1966;
C.R. Martin, Acc. Chem. Res. 28 (1995) 61–68;
C.R. Martin, Chem. Mater. 8 (1996) 1739–1746.
[43] J.-C. Bradley, S. Babu, P. Ndungu, A. Nikitin, Y. Gogotsi, Chemistry Preprint Server 0303002. Available from <http://preprint.chemweb.com/chemistry/0303002>.
[44] H.A. Pohl, Dielectrophoresis: The Behavior of Neutral Matter in Non-uniform Electric Fields, Cambridge University Press, New York, 1978.
[45] T.B. Jones, Electromechanics of Particles, Cambridge University Press, New York, 1995.
[46] J.A. Stratton, Electromagnetic Theory, McGraw-Hill, New York, 1941.
[47] X. Wang, X.B. Wang, P.R.C. Gascoyne, J. Electrostat. 39 (1997) 277–295.
[48] FEMLAB is a product of COMSOLAB, Sweden.
[49] H. Liu, H.H. Bau, in review (2003).
[50] R.E. Ross, Metallic Materials Specification Handbook, fourth ed., Chapman & Hall, New York, 1992, p. 278.
[51] H.O. Pierson, Handbook of Carbon, Graphite, Diamond and Fullerenes – Properties, Processing and Applications, Knovel Interactive Books and Database, 1993. Available from <http://www.knovel.com/knovel2/Toc.jsp?SpaceID=10089&BookID=242>.
[52] G.K. White, J. Phys. D 6 (1973) 2070.
[53] J. Kirchgessner et al., IEEE Bipolar/BiCMOS Circuits and Technology Meeting, 2001, pp. 151–154.